Dislocation dynamics during plastic deformations of complex plasma crystals

C. Durniak,* D. Samsonov,† and J. F. Ralph
Department of Electrical Engineering and Electronics, The University of Liverpool, Liverpool L69 3GJ, England, United Kingdom

S. Zhdanov and G. Morfill
Max-Planck-Institut für Extraterrestrische Physik, D-85741 Garching, Germany

(Received 1 August 2013; published 1 November 2013)

The internal structures of most periodic crystalline solids contain defects. This affects various important mechanical and thermal properties of crystals. Since it is very difficult and expensive to track the motion of individual atoms in real solids, macroscopic model systems, such as complex plasmas, are often used. Complex plasmas consist of micrometer-sized grains immersed into an ion-electron plasma. They exist in solidlike, liquidlike, and gaseouslike states and exhibit a range of nonlinear and dynamic effects, most of which have direct analogies in solids and liquids. Slabs of a monolayer hexagonal complex plasma were subjected to a cycle of uniaxial compression and decompression of large amplitudes to achieve plastic deformations, both in experiments and simulations. During the cycle, the internal structure of the lattice exhibited significant rearrangements. Dislocations (point defects) were generated and displaced in the stressed lattice. They tended to glide parallel to their Burgers vectors under load. It was found that the deformation cycle was macroscopically reversible but irreversible at the particle scale.

DOI: 10.1103/PhysRevE.88.053101 PACS number(s): 52.27.Lw, 52.35.Fp, 52.65.Yy, 62.20.fg

I. INTRODUCTION

Many known solids have a periodic crystalline structure; however, perfect periodicity is often disrupted by various crystallographic defects. These affect significantly mechanical properties of the crystal, such as mechanical strength, elastic modulus, and fatigue resistance, as well as transport properties of the crystal, such as particle and heat transfer. Dislocations, a subclass of defect, are produced by a shift of crystal planes relative to each other or by plastic deformations. They can appear and disappear in response to stress, temperature, and other environmental parameters, thereby modifying many material properties. This makes it interesting and important to study their dynamics in solids.

Various experimental methods have been developed to observe dislocations in real solids [1]. They include surface methods, decoration methods, x-ray diffraction, transmission electron microscopy (TEM), field-ion microscopy, and atom probe tomography. Surface methods visualize the dislocation by treating the surface of a sample, for example, by chemical etching or ion bombardment. If the etching rate is higher in the vicinity of a near-surface dislocation, a visible macroscopic dent is produced. Decoration methods involve the introduction of highly visible impurity atoms into a transparent crystal. These atoms precipitate near dislocations and make them observable with an optical microscope. X-ray diffraction allows the observation of dislocations from the diffraction pattern that they produce. However, these methods do not resolve positions of individual atoms at the dislocation. They can be prone to artifacts and have other limitations, such as size and thickness of the specimen, quality of the surface, allowed range of temperatures, size, and number density of the dislocations. TEM, field-ion microscopy, and atom probe tomography do resolve the positions of individual atoms near the dislocation. They are imaging methods based on electron or ion beams with a much higher resolution than the optical methods. Their limitations include size and stability of the specimen: they produce atomic scale resolution for thin specimen. They might also be destructive for the specimens, and they are in general not very fast, making dynamic studies very difficult if possible.

Computer simulations are widely used to study dislocations, especially to understand their properties, which are not easy to measure experimentally. The simulation of material plasticity should include several length scales: interatomic distances, the mean distance between dislocations, the crystal grain size, and the size of the crystal lattice. The most difficult area to model is the core of a dislocation, which is several interatomic distances thick. This is where deformations are well beyond the linear elasticity theory, and the atomic positions are impossible to measure with high enough precision. Dislocation cores determine the key properties of lattices; thus, it is very important to understand their physics. Several computational methods can be used to model dislocations. *Ab initio* simulations use first principles quantum mechanical equations to describe atomic interactions [2,3]. While very accurate, they are extremely computationally intensive. For example, it was shown with the first principles simulation that the orientation of Stone-Wales defects (pairs of pentagons and heptagons created by 90° rotation of a carbon-carbon bond) close to the edge of graphene nanoribbons could result in compressive or tensile stress [4]. Molecular dynamics (MD) or molecular statics methods use discrete atomistic models described by classical equations of motions [5,6]. While they allow the simulation of much larger lattices, they need a prior knowledge of interatomic potentials from either *ab initio* simulations or experiments. Molecular dynamics simulation has been used to study defects in melting and freezing metal nanoparticles consisting of about 3000 nickel atoms [7]. Continuum methods such as dislocation dynamics

*celine.durniak@liv.ac.uk
†deceased

model string dislocations as line singularities in an elastic or viscoplastic continuum [8,9]. The dislocations are treated as reacting with each other and forming networks with junctions. These three approaches to dislocation simulation work well at their scale domains: *ab initio* at the dislocation core scale, molecular dynamics and statics at the interdislocation and grain size scale, and dislocation dynamics at the crystal lattice scale or engineering component scale.

Dislocations and defects have direct analogies in structured materials studied in various condensed soft matter fields, such as colloids, foams, granular media, and complex plasmas. These materials can form crystalline, quasicrystalline, or amorphous solid structures under certain conditions. Being macro- or mesoscopic, these structures can be observed easily using optical microscopy. Colloids are suspensions of small particles in a liquid. Each individual particle can be tracked in three-dimensional (3D) colloidal systems in space and time [10]. This method has been used to study glass transitions during shear melting in colloidal glasses [11]. Defect dynamics in two-dimensional (2D) colloids during melting have been observed directly by Tang *et al*. [12]. Their analysis indicates that the melting may be a first order process, whereas the correlation analysis was consistent with a continuous two-step melting transition. The topological configurations and dynamics of individual point defect vacancies and interstitials in a 2D crystal of colloids interacting via a repulsive Yukawa potential have been studied by Libal *et al*. [13]. In [14], the authors showed that the hopping of defects does not follow a pure random walk but exhibits some memory effects. Electrically driven colloids are used to investigate defects, melting, and crystallization [15]. Defect dynamics have been studied in 2D charged granular media and showed that the defects form preferentially at the edge of the lattice [16]. Foams have a topology completely different from other kinds of soft matter and atomic solids. Monodisperse foams in the dry limit form polyhedra with flat faces [17], which resemble Voronoi polyhedra in 3D solids. This analogy also holds in 2D cases. Simulated foams are often generated using Voronoi polygons [18]. An example of an irreversible process, often observed in rheology of 2D foams, at the microparticle scale is neighbor swapping or a T1 event. For example, Lundberg *et al*. [19] and Dennin [20] investigated the role of these T1 events in reversible and irreversible macroscopic responses of sheared foams.

One of the soft matter fields, where dislocation dynamics is studied, is complex plasmas. They are multicomponent plasmas containing micron-sized particles or grains, in addition to the usual weakly ionized plasma components. The grains collect electrons and ions, acquire high electric charge, and interact collectively. Complex plasmas are similar to colloids: they exist in solid, liquid, or gaseous states and exhibit phase transitions. Unlike colloids, which are based on liquids, the grains in complex plasmas are exposed to smaller frictional forces due to gas damping. Thus, complex plasmas can sustain waves, solitons [21,22], shock waves [23], phase transitions [24–27], Mach cones [28,29], and other dynamical effects. They can be used as model systems to study dynamic phenomena and physical properties of matter at the kinetic level including dislocation dynamics. A number of order parameters has been proposed to characterize the melting of 2D complex plasmas in [30]. Defect dynamics in a liquid complex plasma have been reviewed by Chan *et al*. considering the effects of thermal agitation, external shear, and structural ordering [31]. The dynamic behavior of dislocations in 2D strongly coupled complex plasmas excited by compressional solitary waves has been studied in [32]. It was found that the dislocations moved either continuously due to elastic deformation of the lattice or jumped between pairs of particles in the lattice in the direction parallel to their Burgers vectors. The data from complex plasma experiments and MD simulations demonstrated that lattice defects induce elastic deformations in the surrounding lattice and disturb the local number density and lattice orientation [33]. Dislocation dynamics were shown by Knapek *et al*. to play a decisive role in determining the nature of a nonequilibrium phase transition [34]. Nosenko *et al*. reported a direct experimental measurement of the relation between glide speed of edge dislocations and the externally applied shear stress in a 2D complex plasma crystal [35]. They observed sub- and supersonic dislocations, with the latter ones playing a central role in shear melting of crystalline solids. Nucleation of dislocations, compact dislocation clusters, and other point defects in a 2D complex plasma crystal have been recently discussed by Zhdanov *et al*. [36]. The dislocation clusters, consisting of "paired" dislocations and, hence, topologically neutral [37,38], are practically immobile under stress. Here we report experimental observations and numerical simulations of dislocation dynamics in a monolayer crystalline complex plasma undergoing a uniaxial cycle of compression and decompression of different strengths. We focused on the behavior of dislocations: their generations and dynamics under different external compressive loads. We show that deformations were structurally reversible at the macroscopic scale but irreversible at the microscopic scale because of plastic deformations at the particle scale due to the dynamics of dislocations. This effect has analogies in material science with effects such as strain aging or annealing, where modifications of dislocation arrangements can improve materials' performance [1].

II. EXPERIMENTAL AND NUMERICAL PROCEDURES

A. Experimental setup

The experiments were conducted in a capacitively coupled radio frequency (rf) discharge as shown in Fig. 1. An argon flow (2 cm^3/min at STP) maintained a constant working gas pressure of 1 Pa in the chamber. A rf power of 2 W was applied to the lower disk electrode, which was 20 cm in diameter. The chamber itself was the other grounded electrode. Monodisperse plastic microspheres with a mass of 6.1×10^{-13} kg and a diameter of 9.19 ± 0.1 μm were injected into the plasma through a particle dispenser. Due to different areas of the electrodes and different mobility of ions and electrons, the powered electrode had a dc self-bias voltage of -92 V, which helped to suspend the microparticles in the plasma sheath against the effect of gravity. The particles were radially confined by a rim on the outer edge of the lower electrode, forming a monolayer hexagonal lattice of approximately 6 cm in diameter. The lattice was illuminated by a horizontal thin (about 0.1 mm) sheet of laser light. All particles stayed within

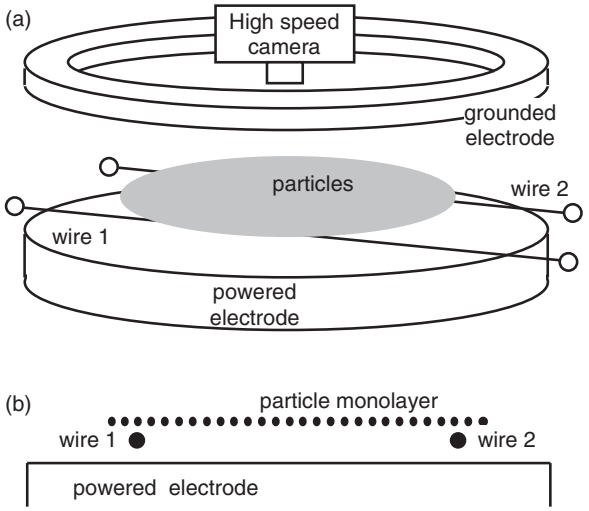

FIG. 1. Sketch of apparatus. (a) Oblique view. Spherical particles charge negatively and form a monolayer levitating in the plasma sheath above the lower electrode. (b) Side view. Two wires placed below the lattice are used to apply the voltage ramps.

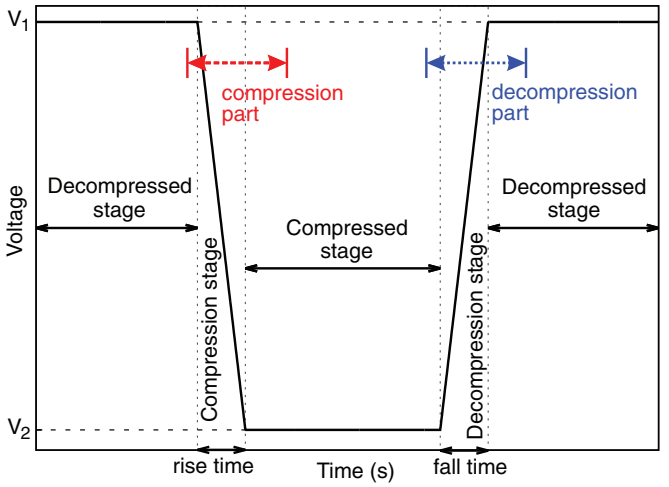

FIG. 2. (Color online) Stages of the experiment and time evolution of the voltage applied to the wires. The initial voltage was $V_1 = -9.6$ V and the compressing voltage was $V_2 = -50$ V. The duration of compression and decompression stages corresponded, respectively, to the rise and fall time, which had equal values set in the range between 1 and 20 s. The durations of the compressed and decompressed stages were approximately equal. The total period of the experimental cycle was 33 or 100 s. The data sets were divided into the compression part [red (light gray) dashed double arrow] and decompression part [blue (dark gray) dotted double arrow] for the purposes of data analysis. The compression part included a small portion of the initial decompressed stage, the compression stage, and a fraction of the compressed stage. The decompression part contained a small portion of the compressed stage, the decompression stage, and a fraction of the final decompressed stage.

the thickness of the sheet. Images of the microparticles were recorded by a top-view digital camera at a rate of 96 frames per second. The field of view, equal to 58×42.58 mm^2, contained between 2235 and 2408 particles (depending on the run). The duration of the recording was set to include the whole compression-decompression cycle.

The crystalline lattice was characterized by an average interparticle distance of 1.025 mm. Two parallel horizontal tungsten wires, both 0.1 mm in diameter, were placed below the particles, symmetrically on both sides of the lattice and 57.4 mm apart [see Fig. 1(b)]. The coordinate system was chosen, so that the x axis was parallel to the excitation force and the y axis was parallel to the wires. The vertical position of the sheet of laser light was adjusted to illuminate well all particles comprising the monolayer [39]. Negative voltage pulses were used to excite compressional disturbances [21,23,40]. In order to compress the lattice uniaxially, we applied a slowly varying voltage ramp simultaneously to both wires. The initial voltage of -9.6 V was linearly changed to -50 V in a given rise time (between 1 and 20 s). It then stayed constant and subsequently changed linearly back to the initial voltage. The negatively biased wires repelled the particles on both sides toward the center of the chamber and thus compressed the lattice. Note that the vertical confinement of the particles did not noticeably change because of the presence of the biased wires [39]. A negative voltage applied to the wires pushed the particles away, as observed in [41], partly breaking the lattice above the wires and creating a horizontal compression, perpendicular to the wires. The monolayer also slightly oscillated with a small amplitude in the vertical direction after the excitation. This temporary loss of particles from the field of view was taken into account and effectively compensated by refining our tracking algorithm, as described below in Sec. II C. Figure 2 shows the stages of the experiment: the initial decompressed stage, compression stage, compressed stage, decompression stage, and again the decompressed stage. The whole cycle repeated with a period of 33 or 100 s in order to allow the lattice to come to an equilibrium and cool down between runs. The compression part [red (light gray) dashed double arrow] and the decompression part [blue (dark gray) dotted double arrow] shown in Fig. 2 corresponded to the analyzed parts of the experimental runs. They started slightly before any variation of the applied voltage and continued for some time after the voltage settled to a new value.

B. Molecular dynamics simulations

Two-dimensional numerical simulations have been performed using a molecular dynamics code described in [23]. It solved the equations of motion of the negatively charged microparticles interacting with all the other microparticles via a force derived from a Yukawa potential $\propto \exp(-r/\lambda_D)/r$, where λ_D is the Debye length and r is the interparticle distance. As we did not impose any boundary conditions on the system, a global confining potential was implemented in order to counteract the repulsive Yukawa interaction: a parabolic potential was used, $U = m\Omega^2(x^2 + y^2)/2$, where m is the particle mass, Ω is the horizontal confining parameter, and x and y are the microparticle coordinates. The particle motion was damped by collisions with neutrals modeled by a friction force expressed as $-m\nu\mathbf{v}$ with a damping rate ν and a particle velocity $\mathbf{v}$. The equations of motion were solved using the fifth order Runge-Kutta method with the Cash Karp adaptive step size control algorithm [42]. The particles were randomly seeded and the code was run without any excitation force in

order to equilibrate the system and to generate a monolayer hexagonal lattice. We then applied excitation forces of different durations and amplitudes to this monolayer and analyzed their evolution. The numerical model allowed us to use exactly the same initial lattice (which is not possible in the experiment) for the numerical runs, which differed by the external forcing conditions.

A complex plasma lattice consisting of 3000 particles was simulated using the following parameters: a particle mass $m = 5 \times 10^{-13}$ kg, a damping rate $\nu = 1$ s^{-1}, a confining parameter $\Omega = 2$ Hz, a constant Debye length $\lambda_D = 1$ mm, and a constant particle charge $Q = 16000e$, where e is the electron charge. The equilibrated lattice was initially characterized by an average interparticle distance of 0.725 mm and a diameter of 50.2 mm. An inward compressing force has been applied simultaneously at both sides of the lattice along the x direction to mimic the wire force in the experiment. Each numerical run consisted of a compression stage, compressed stage, decompression stage, and decompressed stage (Fig. 3). The amplitude of the force started from zero, increased to its maximum value of F_{ex0}, kept its maximum value, reduced back to zero, and stayed zero afterward. The compression and decompression stages of the excitation each lasted τ seconds and followed a parabolic temporal profile. The compressed and decompressed stages had equal duration, so that the whole cycle lasted 40 s. The spatial profile of the excitation force (independent on the y coordinate) was composed of two semi-infinite Gaussian transitions with a waist w of 2 mm—$\exp[-(x + x_0)^2/w^2] - \exp[-(x - x_0)^2/w^2]$ for $|x| \leqslant x_0 = 12$ mm—and it was equal to 1 otherwise. The

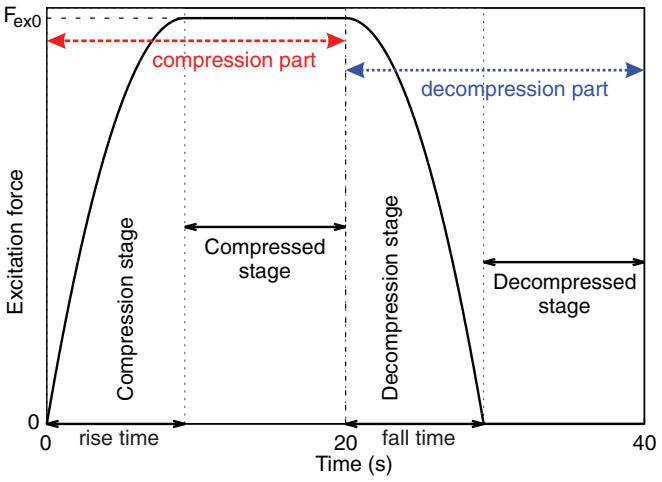

FIG. 3. (Color online) Stages of simulation and temporal evolution of the excitation force in the simulations. F_{ex0} was the amplitude of the excitation force and it varied between 0.05 and 1 arb. unit. The rise and fall time τ corresponded to the duration of the compression and decompression stages. These times were equal to each other and varied between 2.31 and 13.86 s depending on the numerical run. The total period of the numerical cycle was 40 s. The data sets were divided into the compression part [red (light gray) dashed double arrow] and decompression part [blue (dark gray) dotted double arrow] for the purposes of data analysis. The compression part consisted of compression and compressed stages. The decompression part contained decompression and decompressed stages.

lattice responded to these variations of the applied load, first by a displacement of the particles in the direction parallel to the force toward the center of the lattice to reach the compressed state and second by a motion in the outward direction to reach the decompressed stage. We varied the duration τ and the force amplitude F_{ex0} to produce multiple numerical runs. The force amplitude is reported below in normalized units $4\pi\epsilon_0 m\lambda_D^2/Q^2$, where ϵ_0 is the vacuum permittivity. The data analysis was performed for the numerical runs split into the compression part [red (light gray) dashed double arrow] and decompression part [blue (dark gray) dotted double arrow] (Fig. 3) in order to facilitate comparison with the experiments.

C. Particle and defect tracking

The experimental data were analyzed by identifying the particle positions and tracking them in consecutive frames. In order to perform an accurate analysis of defect dynamics in the experimental runs, we had to take special measures in order to reduce the number of misidentified or lost particles. The video images were preprocessed [43] to remove the stationary background. First, all video frames in the sequence were averaged and blurred with a Gaussian filter. The image pixels were compared to the corresponding pixels of the background and set to zero if their values were below. Second, we applied a small fixed threshold to all images in order to remove any residual random noise. Third, morphological operations of opening and closure [44] were applied to the binary template of the image in order to connect bright objects with small gaps in between and thus prevent particle fragmentation. The particle identification was performed using an intensity weighted moment method and following the recommendations of [45,46] in order to reduce the pixel locking. We used a particle tracking velocimetry algorithm instead of a more advanced method based on an extended Kalman filter [47] due to its significantly lower computational cost. This was essential for analyzing numerous long experimental runs. The tracking algorithm [21] has been refined by introducing a multiframe tracking, which would find and link particles that were lost for a few frames and then reappeared later. These simple measures have significantly improved the particle tracking reliability and thus reduced the incidence of falsely identified lattice defects.

Crystal cells of a stable ideal 2D lattice have a sixfold symmetry; in other words, each central particle has six nearest neighbors. Particles with another number of nearest neighbors form defective cells. The most common are fivefold (penta) and sevenfold (hepta) defects. In a lattice with a low defect density they usually form pairs: penta-hepta defects (PHDs) or dislocation [32]. The deformation affected by a dislocation might be thought of as being caused by the insertion of an extra half line of particles to the ideal hexagonal lattice [48]. Each dislocation is characterized by its Burgers vector **b**, which is nearly orthogonal to the line connecting the centers of the fivefold and sevenfold cells and the length of which is equal to the lattice constant [49]. The Burgers vector quantifies the distortion of the lattice by the dislocation, and it can be considered as the dislocation's topological charge [8].

It has been observed that dislocations can either move in small increments following the lattice particles due to elastic deformation or jump from one pair of particles to the next [32].

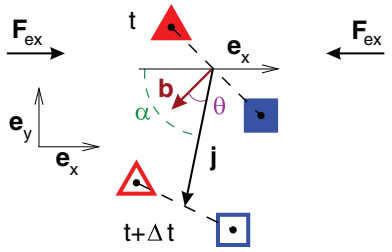

FIG. 4. (Color online) Schematic diagram of a dislocation jump from the initial state at time t to the final at $t + \Delta t$. The lattice is compressed by an external force $\mathbf{F}_{ex}$ applied to the opposite edges of the lattice along the x axis. The filled triangle (▲) and square (■) indicate the initial position of the fivefold and sevenfold defects, respectively. The open triangle (△) and square (□) mark the final position of the fivefold and sevenfold defects, respectively. The position of the dislocation is calculated as the midpoint of a line connecting the fivefold and sevenfold defects, also known as the barycenter. The dislocation displacement vector (i.e., jump) **j** joins the old and the new positions of the barycenter. The angle α characterizes the absolute direction of the dislocation jump. It is the angle between the displacement **j** and the x axis. The angle θ is the angle between **j** and the Burgers vector **b** of the dislocation.

This makes dislocation tracking not very straightforward even in the simulation, where the identities of all lattice particles are known [36]. Our dislocation tracking algorithm is somewhat similar to the particle tracking velocimetry procedure. First, the dislocations were identified using Delauney triangulation, and pairs of particles with five and seven nearest neighbors were found. Second, we checked the presence of defective cells around a PHD in order to identify it as isolated [50]. It should be noted that more complicated methods are used to identify dislocations in 3D lattices [51]. Third, the dislocations were tracked by finding a nearest isolated dislocation in the next frame. This took into account that the dislocations were not permanently associated with the lattice particle but were able to jump between them. The algorithm then calculated the displacement of all isolated PHDs between consecutive frames. If the dislocation disappeared or came into close contact with another one and became nonisolated, it was discarded by the tracking program. Newly appearing PHDs were also tracked as long as they became isolated. This procedure provided reliable tracking of jumping isolated dislocations and allowed us to reconstruct their trajectories in the 2D lattice.

In order to fully characterize dislocations, the tracking program also calculated their Burgers vectors **b**, the displacement vector (i.e., jump or glide) **j**, the angle α between **j** and the x axis, and the angle θ between **j** and **b** (Fig. 4). The angle α characterizes the absolute direction of the dislocation motion. It varies in the range $\pm 90^\circ$ since the force is applied symmetrically from both sides. The angle θ shows the relative direction of displacement with respect to the Burgers vector. It changes in the range $\pm 180^\circ$.

III. RESULTS AND DISCUSSION

A. General observations

Here we summarize some of the key facts observed during uniaxial compression of complex plasma crystalline lattices. These observations were qualitatively identical in the experiments and in the simulations, so that the discussion will equally apply to both, unless a distinction is made explicitly.

The initial lattice had mostly regular hexagonal structure with some isolated dislocations and defect chains [Fig. 5(a), where we can count 28 isolated dislocations in the initial configuration of the lattice generated numerically]. The presence of defects resulted from the interplay between different symmetries: the Yukawa interparticle interaction favored a hexagonal structure, whereas the global parabolic confinement induced a circular symmetry. The simulated lattice had a circular shape initially. The experimental initial lattice was bound by the wires; therefore, it had the shape of a slab with two linear sides and two rounded; the camera view cropped the lattice in the y direction keeping the middle part and showing its full extent in the x direction. As the excitation force was applied, the lattice was compressed uniaxially in the x direction and simultaneously elongated in the y direction becoming ellipselike [Figs. 5(b) and 5(c)]. When the compressing force was released, it returned to its original shape after decompression [Figs. 5(d) and 5(e)]. This macroscopic reversibility, however, did not hold at the microscopic level. Individual particles were moved along the x axis toward the lattice center by the compressive force, and the final distribution of defects was distinctly different in each experimental and each numerical run. Faster compression rates generated more lattice defects [Fig. 5(b)] than the slower ones [Fig. 5(c)]. However, the final defect density after decompression and cooling was in general independent on the compression rate, as discussed below in Sec. III B.

Lattice compression caused enhanced mobility of newly generated and existing defects. New defects were produced in pairs as dislocations (PHDs) via shear slips. A more detailed discussion about defect generation is given in Sec. III C. Isolated dislocations tended to move under strain faster and over longer distances than chains or clusters of defects (see Sec. III D). PHDs with opposite orientations of their Burgers vectors annihilated after collisions. Another mechanism of defect loss was at the edges of the lattice.

B. Fraction of dislocations in lattices under compression

After a compressional excitation force was applied to the lattice, the latter responded by deforming. Initially the deformation was elastic; i.e., no defects were generated or moved. As the elastic limit was exceeded, the number of dislocations sharply increased. Figure 6 shows experimental production of isolated dislocations under compressional load. The temporal evolution of the applied excitation for compression and decompression is shown in Figs. 6(a) and 6(b), respectively. Figures 6(c) and 6(d) show corresponding time evolutions of the fraction of isolated dislocations. The number of PHDs rose after a small delay in both cases of compression and decompression, reaching roughly the same maximum value. After the maximum fraction of isolated dislocations was reached, it persisted for some time before it slowly returned to a low equilibrium value, similar to the one at the beginning of the experiment. The number of dislocations produced by

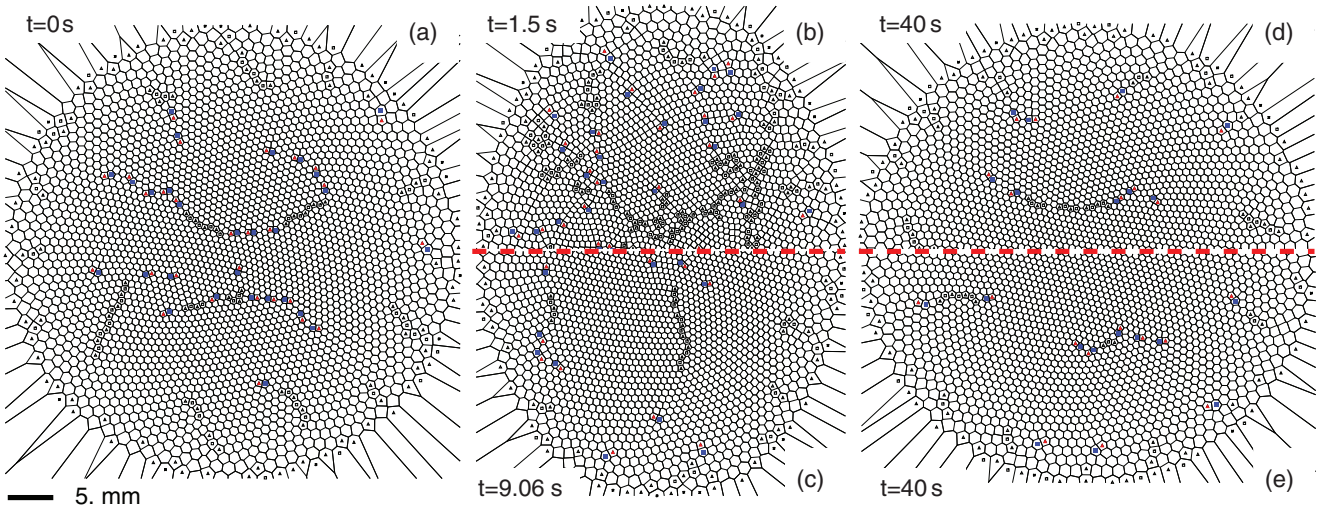

FIG. 5. (Color online) Simulated crystal structures for fast and slow compression/decompression. The figures show Voronoi maps with the lattice defects marked by squares □ (sevenfold) and triangles △ (fivefold). Defects forming isolated dislocations are highlighted by filled squares ■ (sevenfold) and triangles ▲ (fivefold). The centers of sixfold lattice cells are not marked for clarity. The same initial equilibrated lattice (a) was used for all simulations. The lattice structure near the end of the compression stage is shown for fast compression $\tau = 2.31$ s in (b) and for slow compression $\tau = 11.55$ s in (c). The faster compressed lattice exhibits more defects. The final decompressed stage at the end of the simulation cycle has a similar defect fraction for fast (d) and slow (e) decompression.

the load increased as the rise or fall time of the excitation decreased in most cases. This resulted in few PHDs generated by slow excitations (such as $\tau = 20$ s) and many by the shorter ones. The only exception in the trend was the case of $\tau = 3.3$ s. It had a shorter cooling time between the runs: 33 s instead of 100 s compared to other compression rates, which could have resulted in a lower quality of the initial lattice and thus enhanced the defect production. It also had a slightly higher initial proportion of dislocations, which associated with the strong perturbation could have enhanced the generation of new ones. We calculated the height of the first peak of the particle pair correlation function for all our experimental runs in order to characterize the quality of the lattice. Its value was 4.3 for the case of $\tau = 3.3$ s and between 8.5 and 9.8 for all other cases. Note that a high value of this first maximum is characteristic of a highly ordered (crystalline) state, as seen in [52].

As the density of generated dislocations increased, more of them had a chance to interact with one another, forming chains and clusters of defects. In order to characterize this clustering, the fraction of isolated dislocations was plotted as a function of the total number of lattice defects [Fig. 6(e)]. We counted each dislocation as a pair of defects; thus, if all dislocations were

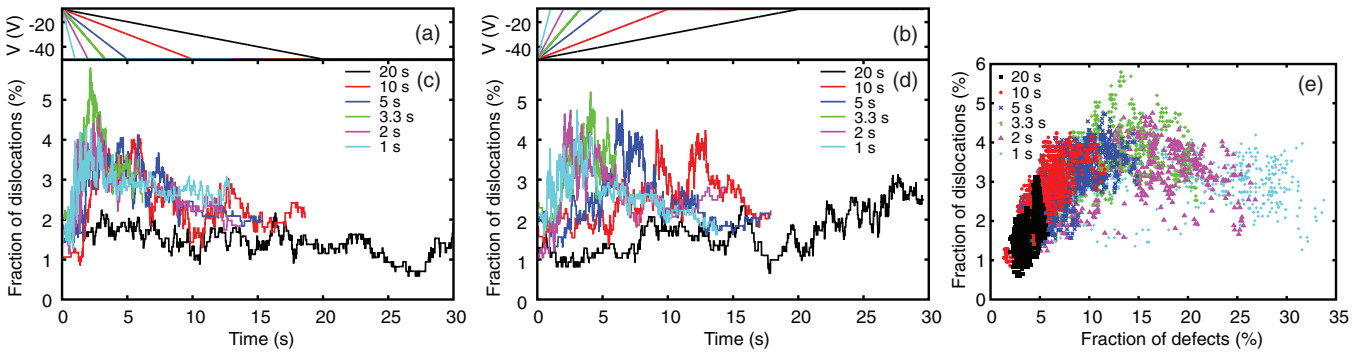

FIG. 6. (Color online) Experimentally measured fractions of isolated dislocations during compression and decompression parts of uniaxial load cycles. Time evolution of compressing and decompressing excitation voltages is shown in (a) and (b), respectively. The initial and final voltages remained the same for all experiments, while the rise and fall time of the voltage ramp varied. The dislocation fraction time series were aligned at the beginning of compression (c) and decompression (d) stages for easy comparison. It was found that the dislocation fraction started increasing soon after the voltage ramp was applied and stayed elevated after the end of the ramp before decreasing to the initial value. Shorter excitations resulted in more dislocations generated. The fraction of isolated dislocations vs the total fraction of lattice defects (e) plotted for all experiments shows a growth followed by a saturation and a decline of the dislocation fraction. This happens because at high defect densities more dislocations cease to be isolated and join others to form clusters and chains. In our system a defect is a microparticle with a number of nearest neighbors different from six. An isolated dislocation is defined as a pair of fivefold and sevenfold defects (a microparticle with, respectively, five and seven nearest neighbors) not in direct contact with any other defective microparticle. On average, 44% of defects formed isolated dislocations.

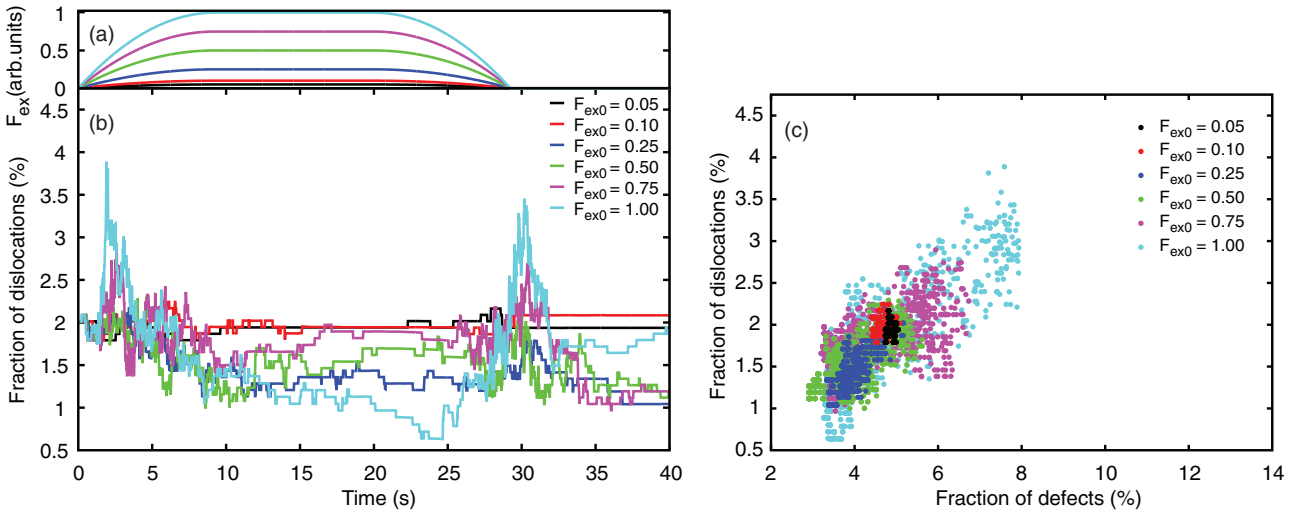

FIG. 7. (Color online) Simulated fractions of isolated dislocations measured during compression and decompression parts of uniaxial load cycles. (a) Time evolution of the compressing and decompressing excitation force F_{ex}. The amplitude of the excitation F_{ex0} was varied, while the rise and fall time remained the same for all numerical runs. It was found that the dislocation fractions (b) started increasing soon after the force ramp was applied and stayed elevated after the end of the ramp before decreasing to the initial value or even below it. Higher amplitude excitations resulted in more dislocations generated. The fraction of isolated dislocations vs the total fraction of lattice defects (c) plotted for all runs shows a proportional growth. The excitations were too weak to observe a clear saturation phenomenon.

isolated, the total number of defects would be twice the number of PHDs. The fraction of defects (dislocations) was calculated with respect to the total number of lattice sites. Figure 6(e) shows that as the total fraction of defects increased the fraction of isolated dislocations started saturating and finally dropped off below the maximum value of about 6%. This indicates that more defects clustered at higher defect fractions.

Similar trends of defect behavior were observed in the simulations. Here we investigated the effects of different amplitudes (Fig. 7) and different rise and fall times of the excitation force (Fig. 8). As in the experiments, the fraction of isolated PHDs increased following a small delay after the compression (decompression) force was applied. It then reduced to the initial value or below some time after the excitation force became constant (compressed and decompressed stages).

Figure 7(a) shows the applied excitation with varying amplitude F_{ex0}, and Fig. 7(b) shows the corresponding time evolution of the fraction of isolated dislocations. The maximum number of isolated PHDs increased roughly with the amplitude of the applied excitation. Since the initial lattice was the same in each series of simulated runs, we could unambiguously observe an effect of lattice annealing, when the final number of isolated dislocations was lower than the initial one. This effect was more pronounced for stronger excitations. It also appears to have a threshold value. The lowest perturbation amplitudes produced no visible annealing, while generating defects during compression (decompression). Figure 7(c) presents the fraction of isolated PHDs as a function of the total number of defects. The saturation is less pronounced than in the experiment due to weaker excitations.

The effect of the rise and fall time of the excitation τ is presented in Fig. 8. Figure 8(a) shows the variation of the perturbation, and Fig. 8(b) shows the corresponding time evolution of the fraction of isolated dislocations. The maximum fraction of isolated PHDs increases as the rise (fall) time decreases, reproducing the results of the experiment. Since the relaxation times in complex plasmas are of the order of 0.1 s, compression rates of 1–3 s are equivalent to those produced by shocks or ultrashort laser pulses. Shehadeh *et al*. have investigated ultrashort wave propagation caused by shocks in copper single crystals and how they produce plastic deformation and interact with dislocations [53]. It was found that if a pulse of constant pressure was used for compression the dislocation density increased with the pulse duration up to a threshold beyond which the density saturated. For our system, a saturation was also observed for the shortest rise (fall) time, as shown in Fig. 8(c).

C. Generation of dislocations by deformations

In this section we discuss how dislocations are produced at the microscopic level. Initially, when the applied force was below the elastic limit, the lattice cells deformed elastically. As the force grew larger, the deformation became plastic due to irreversible microscopic effects such as defect production under strain, their mobility, and interactions. The most interesting fact observed previously is that while the applied deformation is compressive the lattice fails via a shear slip [39]. This can be explained by the fact that a uniaxial compression is a superposition of "more elementary" uniform compression and shear. It is relatively easy to compress complex plasmas uniformly. The only limitation is the vertical lattice stability in quasi-2D lattices (experiment) [54]. Our experiments were conducted under conditions ensuring vertically stable lattices. True 2D lattices (simulation) do not have this limitation. As the uniform compression is absorbed elastically by reducing

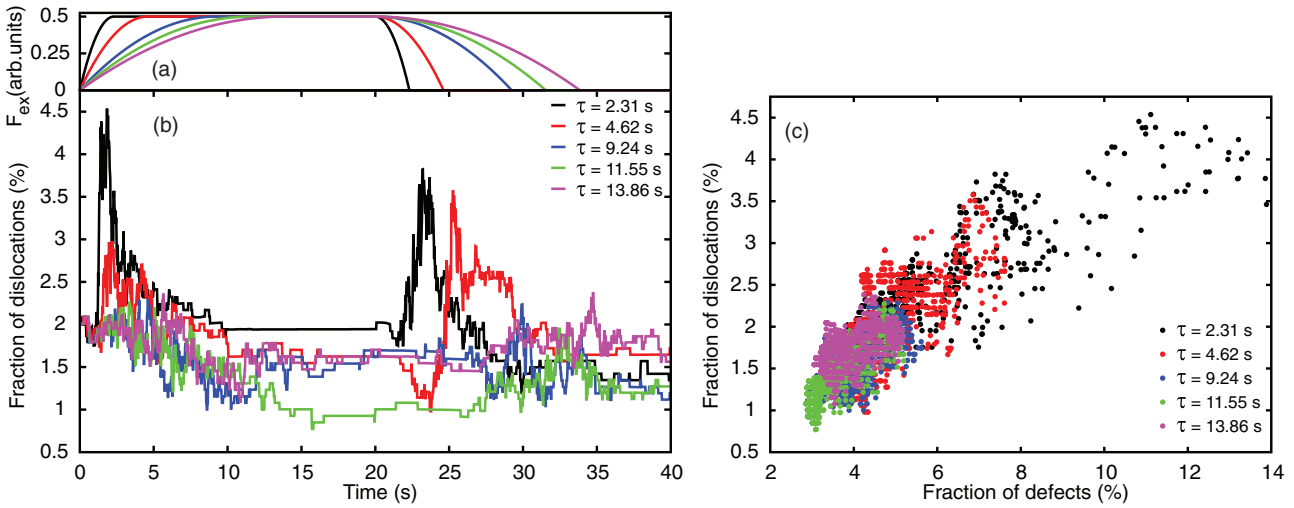

FIG. 8. (Color online) Simulated fractions of isolated dislocations measured during compression and decompression parts of uniaxial load cycles. (a) Time evolution of the compressing and decompressing excitation force F_{ex}. The amplitude of the excitation force remained the same for all numerical runs, while the rise and fall time τ was varied. It was found that the dislocation fractions (b) started increasing soon after the force ramp was applied and stayed elevated after the end of the ramp before decreasing to the initial value or even below it. Shorter excitations resulted in more dislocations generated. The fraction of isolated dislocations vs the total fraction of lattice defects (c) plotted for all runs shows a nonlinear dependence, as observed in the experiments [see Fig. 6(e)] for the shortest rise (fall) time τ of the excitation force. This happens because at high defect densities more dislocations cease to be isolated and join others to form clusters and chains resulting in a nonlinear dependence which tends to saturate.

the average interparticle distance, the shear strain accumulates [39]. When the shear exceeds the elastic limit, it is relieved by one of the following irreversible deformations: shear slip, enhanced dislocation mobility, or interactions of preexisting dislocations. Only the first of these processes results in the generation of new dislocations. Apart from shear slips, PHDs are generated by direct heating of the lattice [55,56]. This effect is more pronounced for the short excitation pulses in our experiments and simulations. Dislocations can also be emitted from grain boundaries or disappear by recombination [31].

Shear slips are displacements of particles in neighboring lattice rows in opposite directions by one (or more) interparticle distance. They generate pairs of dislocations moving in opposite directions [39,57] and increase the number of lattice defects. Nosenko *et al*. described dislocation nucleation during a shear slip in [58], which is a complicated four-stage process. The generation of dislocation pairs under high stress has been also observed by Chen *et al*. in carbon nanotubes [59]. Effects of instantaneous strain on polymer glasses have been studied by Wallace and Joos using molecular dynamics simulation [60]. Two regimes were separated: elastic for small deformations and plastic for large ones. Irreversible collective processes have been studied in the plastic regime, such as "jumps" and system relaxation. These results can be applied to understand the yield strength and material aging. The dynamics of dislocations will be discussed in the following sections.

D. Dislocation dynamics

This section discusses how dislocations move and interact with each other under strain. We focus in particular on the characterization of the dislocations' jumps. The first section illustrates the dislocations' trajectories, which are compared with the average motion of all particles during jumps as well as during elastic deformations. Then we analyze the direction of these jumps with respect to the direction of the external load, i.e., the excitation force, and to the dislocation's Burgers vector **b** by considering the angles α and θ between these different vectors, as defined in Fig. 4.

It was observed that dislocations exhibited enhanced motion under strain. Two types of displacement were observed: a smooth elastic displacement for low amplitude strains and jumps or glides for high amplitude strains [32]. The PHDs stayed with the same pair of lattice particles during the smooth elastic motion and followed the deformation of the lattice imposed by the external load. For these displacements the PHDs were "immobile" with respect to the lattice; this motion was reversible. For jumps, the dislocations could also displace from one pair of lattice particles to a neighboring one during jumps. The amplitude of these jumps was close to the lattice spacing, and its direction was either parallel or antiparallel to the Burgers vector of the PHD, as will be discussed in Sec. III D4. Isolated dislocations propagated mostly in one direction and with almost constant speed under compression or decompression. Dislocation jumps or hopping have been also observed in 2D colloidal systems [14]. PHD motion under strain is also a frequent subject of atomistic computer simulations with various interatomic potentials such as the Lennard-Jones or semiempirical embedded atom method [61].

Although our work mostly focused on isolated dislocation, some observations were made of interacting PHDs. When a pair of dislocations with antiparallel Burgers vectors collided,

they were annihilated in a process opposite to a shear slip. Pairs of colliding PHDs with other Burgers vectors orientations would form a cluster and slow down or even stop. More complicated dislocation arrangements such as multijunctions, chains, grain boundaries, or clusters could also immobilize isolated PHDs very effectively. Similar behavior has been observed in dislocation dynamics simulations [36,62,63]. Mobility of dislocations strongly influences the properties of materials, and their mutual interactions have significant contribution to their mobility [64].

1. Dislocations' trajectories

We now explore the statistics of the dislocations' trajectories in the lattice. Figures 9 and 10 show the temporal evolution of all dislocations' displacements Δr during elastic deformations (first column) and jumps (second column) as well as the dislocations' trajectories (third column), respectively, for two experimental and four different simulated cases. We compared extreme experimental and simulated cases: minimum and maximum values of the rise and fall time (i.e., 3.3 and 20 s) in the experiment and minimum and maximum values of the duration (i.e., 2.31 and 13.86 s) or amplitude (i.e., 0.05 and 1 arb. unit) of the excitation force in the simulation. We have considered the dislocations' jumps and elastic displacements separately.

Elastic displacements of the dislocations shown in Figs. 9(a), 9(d), 10(a), 10(d), 10(g), and 10(j) followed the variations of the global lattice deformation (solid line), characterized by the average displacement of all particles. The amplitudes of these elastic displacements increased with the amplitude of the force or as the duration of the compression and decompression stages was shorter. In the experiments, for a rise time of 3.3 s the dislocations' displacement could be up to a factor 2 larger than the average particle displacement. The second experimental case with a longer rise time case was "noisy" during all the analyzed parts of the run; the movement of the dislocations could be up to three times the average particle displacement. In the simulations the largest displacements occurred when the lattice was perturbed by a varying external excitation force, i.e., during the compression and decompression stages, shown with the double arrows. Large amplitude displacements corresponded to dislocations closer to the edge where the particle number density was lower [21]. Not all dislocations were mobile, as the displacements could be close to zero between consecutive time steps. These small displacements were due to the motion of dislocations close to the center of the lattice, where the compressive or decompressive load did not act immediately, or they occurred during the compressed and decompressed stages when no variable strain was imposed on the lattice.

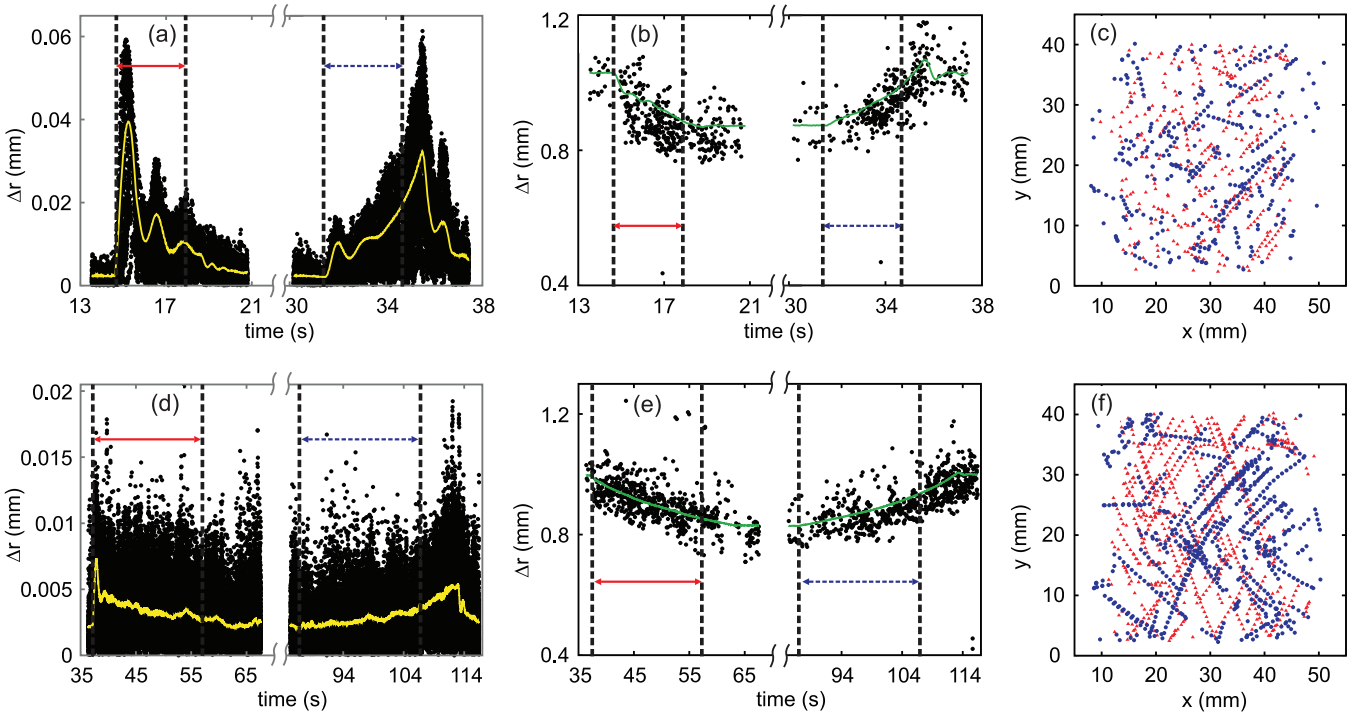

FIG. 9. (Color online) Displacement of dislocations in two experiments with different rise and fall times equal to 3.3 and 20 s, respectively for the first and second line. (a, d) Displacement of dislocations during elastic deformations (jumps excluded). The continuous line corresponds to the average displacement of all particles from frame to frame. (b, e) Amplitudes of the jumps, which also include the overall deformation of the lattice. The continuous curve corresponds to the temporal evolution of the average interparticle distance. (c, f) Positions of "jumping" PHDs (after the jump). The red (light gray) triangles ▲ [blue (dark gray) points •] correspond to jumps occurring during part I covering the compression stage (part II covering the decompression stage). The initial lattice size (area recorded by the video camera) was $x \in [0,55]$ mm and $y \in [0,42.5]$ mm. The double arrows correspond to periods of the experimental runs when the applied force was varying (compression and decompression stages), whereas the white background is associated to a constant load (maximum or minimum, compressed and decompressed stages), as illustrated in Fig. 2.

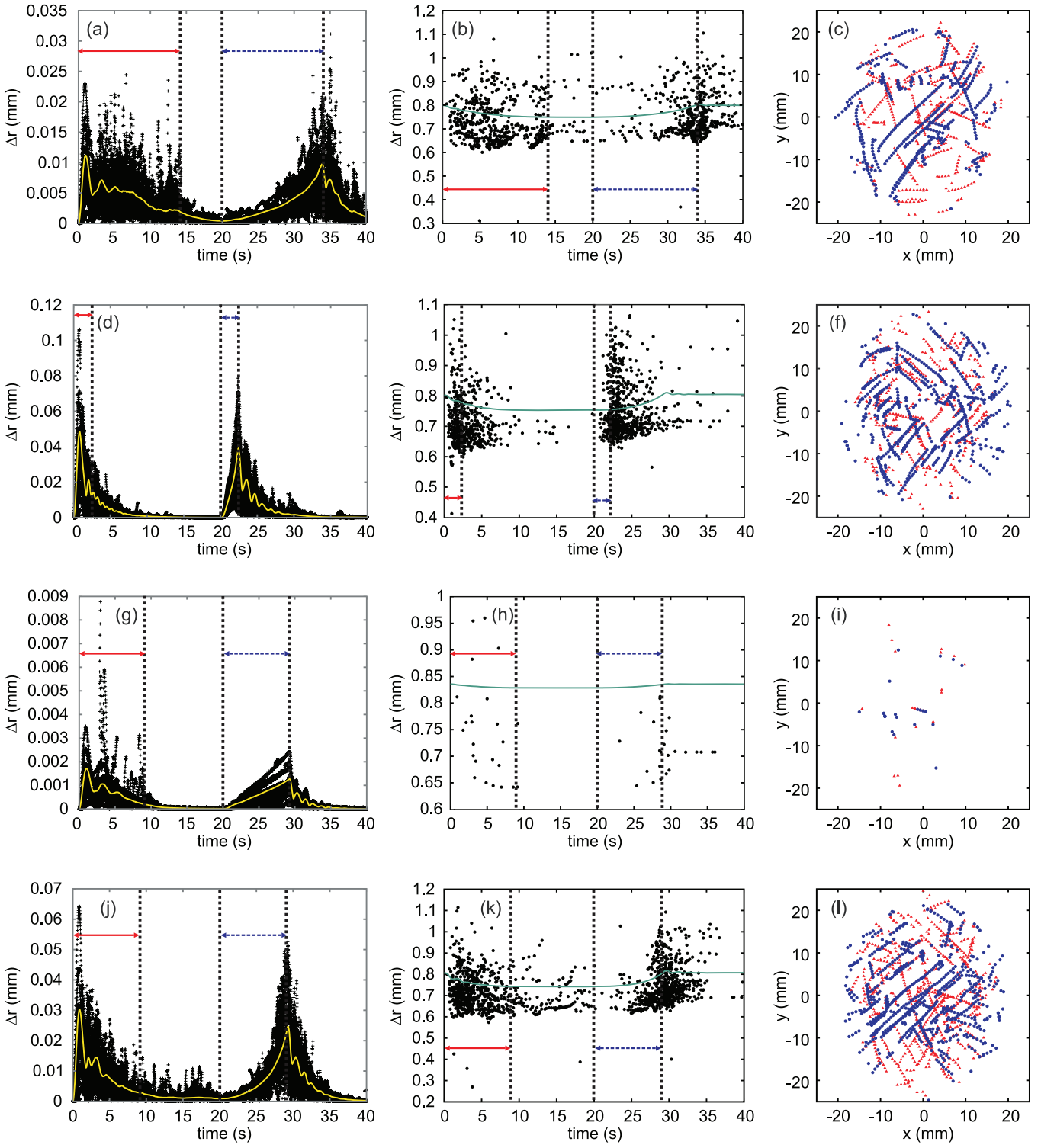

FIG. 10. (Color online) Displacement of dislocations in the simulation for different amplitudes and durations of the excitation force. (a–c) $F_{ex0} = 0.5$ arb. units and $\tau = 13.86$ s. (d–f) $F_{ex0} = 0.5$ arb. units and $\tau = 2.31$ s. (g–i) $F_{ex0} = 0.05$ arb. units and $\tau = 9.24$ s. (j–l) $F_{ex0} = 1$ arb. units and $\tau = 9.84$ s. (a, d, g, j) Displacement of dislocations during elastic deformations (jumps excluded). The continuous line corresponds to the average displacement of all particles from frame to frame. (b, e, h, k) Amplitudes of the jumps, which also include the overall deformation of the lattice. The continuous curve corresponds to the temporal evolution of the average interparticle distance. (c, f, i, l) Positions of "jumping" PHDs (after the jump). The red (light gray) triangles ▲ [blue (dark gray) points •] correspond to jumps occurring during the compression and compressed (decompression and decompressed) stages as illustrated in Fig. 3. The initial configuration of the lattice as illustrated in Fig. 5(a) was circular with a radius of 50.2 mm centered on the origin. The double arrows correspond to periods of the simulations when the applied force was varying (compression and decompression stages), whereas the white background is associated to a constant load (maximum or minimum, compressed and decompressed stages; see Fig. 3).

The PHDs' jumps or glides, which occurred when the dislocations jumped from a pair of microparticles to a neighboring one, followed the evolution of the average interparticle distance (solid line in the second column of Figs. 9 and 10). The points outside this trend corresponded, in the case of small amplitude jumps, to rotations of dislocations, which were close to a network of dislocations or "sandwiched" between defective areas, in a highly deformed lattice structure. In contrast, jumps of high amplitude corresponded to dislocations moving close to the edge of the lattice, where the number density was lower [21]. The amplitudes of these glides were between 6 and 20 times higher than the displacements during elastic deformations: they were comprised between 0.6 and 1.2 mm for the experiments and between 0.6 and 1.1 mm for the simulations. As the dislocations jumped, they could disappear as they interacted with other dislocations with opposite Burgers vectors [31]. They could also form clusters or lines of defects [33].

In the simulations, we observed bursts in the amplitudes of the jumps initiated by variations of the external excitation force during the compression and decompression stages. The number of jumps during the decompression stage (when the load was varied) was lower by 46 to 50% in the simulations and by 24 to 38% in the experiments compared to the initial compression stage. We also noticed an increase in the number of jumps with the amplitude of the excitation force F_{ex0} as reported in [32] for the study of the interaction between dislocations and solitary waves. The evolution of the number of jumps with respect to the duration τ was more complicated: it first decreased as τ was increased up to 9.24 s and then it increased for larger durations. As mentioned in [65], this suggests that there are several relevant rates related to the material, for example, the rate of increase of dislocation density and the rate of plastic relaxation. For $F_{ex0} = 0.05$ arb. unit, the number of dislocations was rather small and the number of jumps was equal to 48 in total. The statistics were therefore very dependent on the localization of these defects in the lattice. For example, the peaks at $t \sim 3$ s in Fig. 10(a) correspond to the dissociation and further displacements of two dislocations close to the edge of the lattice.

The third columns of Figs. 9 and 10 show dislocations' trajectories during the compression and decompression parts in the experiments and simulations, respectively. As the compression was applied from both sides of the lattice during a large duration of the numerical and experimental runs, we did not generate any finite-size perturbation propagating in the lattice, which could have been reflected at the edge of the lattice and later could have complicated the dynamics of our systems, as the dislocations would have been submitted to a successive forward-backward series of perturbations. This case was reported by Robles *et al*. using 2D MD simulations of Lennard-Jones systems [66]. The authors could distinguish three phases in the dislocation motion: the first one was just after the interaction with the perturbation, the second one corresponded to a released period at the end of which the dislocation stopped moving, and the last one was associated to the second interaction with the reflected wave. By using a uniaxial compressive force described in the previous sections, we ensured that the lattice was submitted to a compressive load followed by its gradual relaxation.

The dislocations' trajectories were mostly at an angle compared to the load direction (see Sec. III D3). This behavior was also observed by Pertsinidis and Ling in 2D colloidal crystals during viscoplastic deformations [38]. The dislocations were more mobile when the lattice was submitted to high amplitude or short duration perturbations. The length of their trajectories increased as the perturbation was reduced by increasing the rise and fall times in the experiments or the duration of the force τ or by reducing the amplitude of the excitation force F_{ex0} in the simulations since fewer defects were generated, which could potentially interact with mobile dislocations, preventing their further displacement. We also noticed that there was no preferential localization of the dislocations' motion in the lattice for sufficiently high external loads; the jumps occurred over the whole lattice area. This effect was also reported by Devincre *et al*. in [67]. The authors used 3D dislocation dynamics simulations to investigate the influence of the dislocations' mean free path, i.e., the distance traveled without any interaction with other defects, on strain hardening properties of crystalline structures submitted to tensile deformations. They observed bursts in the dislocations' motion as well as dislocations avalanches in all parts of the crystals. Dislocations avalanches were also experimentally observed using acoustic emission on ice crystals [68], where the authors studied the influence of temperature and microstructure on the dynamics of these avalanches. Finally, in our experiments and numerical simulations of complex plasma crystals under compressive loads, the trajectories during the decompression and decompressed stages did not overlap with the initial compression and compressed motion: the microscopic deformation was irreversible and plastic.

2. *Dislocations' flow*

The dynamics of dislocations have been characterized experimentally and theoretically mostly by the analysis or observations of glides or climbs (in three-dimensional systems) of dislocations [1]. In this section we consider the glides or jumps of isolated dislocations, whose absolute amplitudes were given for the two experimental and four numerical cases, respectively, in Figs. 9(b), 9(e), 10(b), 10(e), 10(h), and 10(k). For this analysis we subtracted the lattice deformation in the neighborhood of each gliding dislocation to calculate the "corrected" amplitudes of the jumps Δr_{cor} for all analyzed experimental runs (six cases) and all numerical simulations (five with varying rise time τ and 6 with varying amplitude F_{ex0}). These jumps occurred between two successive time frames.

Figure 11 shows the histograms of the distribution of this dislocation jump's corrected amplitude. In the experiments the most probable value of Δr_{cor} was equal to 0.85 and 0.97 mm during compression and decompression, respectively. For the simulations, varying duration or amplitude of the excitation force, the most probable amplitude was 0.65 mm for the compression and 0.69 mm for the decompression. These values were in good quantitative agreement with the averaged interparticle distance (over all experimental or simulated cases,

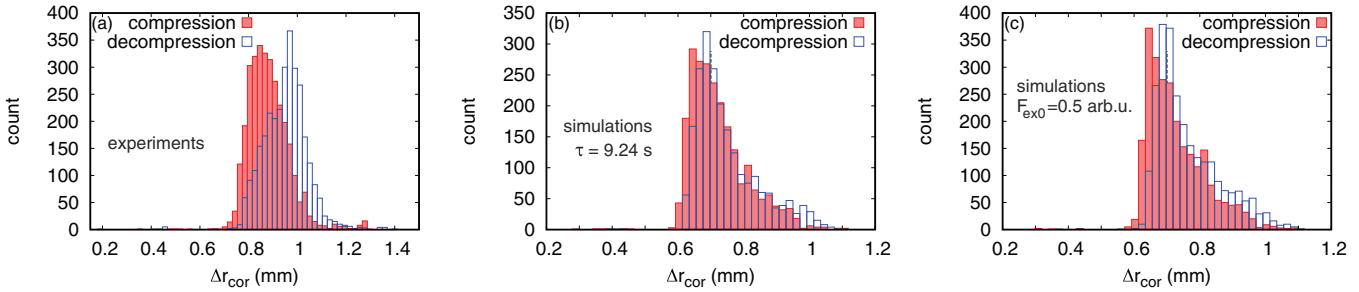

FIG. 11. (Color online) Histograms of the "corrected" isolated dislocations' jumps $\Delta r_{\rm cor}$ (i.e., amplitude of the jump minus local lattice deformation). (a) Experimental runs with the rise and fall time of $\tau = 1$, 2, 3.3, 5, 10, and 20 s. (b) Simulation runs with the rise and fall time of $\tau = 9.24$ s and the excitation amplitudes of $F_{\rm ex0} = 0.05$, 0.1, 0.25, 0.5, 0.75, and 1.0 arb. unit. (c) Simulation runs with the excitation amplitude $F_{\rm ex0} = 0.5$ arb. unit and the rise and fall time of $\tau = 2.31$, 4.62, 9.24, 11.55, and 13.86 s. The histograms were obtained using 60 bins for the experimental results and 40 bins for the simulations, resulting in a bin width of 0.021 mm.

over the whole duration of the compression and decompression parts, and over the whole lattice), which is equal to 0.93 mm in the experiments and 0.77 mm in the simulations. This behavior was also observed by Nosenko *et al.* [see Figs. 2(a) and 2(b) of Ref. [35]] in complex plasma crystals submitted to shear stress. The authors also noticed two regimes for the speed of the dislocations depending on how defective the area they were moving toward was. In our case the larger difference observed in the simulations is due to a more inhomogeneous lattice, where the interparticle distance could vary by up to 90% between the center of the lattice (more dense) and its edge. The absence of any overlap between compression and decompression parts emphasizes the occurrence of plastic deformations in the experiments and the simulations.

3. Direction of dislocations' jumps with respect to the excitation force

Figure 12 shows the histograms of the distribution of angles α between the dislocation's jump direction and the external load direction during the compression part (first line) and the decompression part (second line) in, respectively, (a, d) all experimental runs (six runs) and in the simulations for all different values of (b, e) the amplitudes $F_{\rm ex0}$ (six runs) and (c, f) the durations τ (five runs) of the excitation force. We counted all jumps of PHDs during each run and then binned the values of angle α in 72 bins covering the range $[-90^\circ, 90^\circ]$. We compiled all cases in which a single characteristic parameter of the excitation force, i.e., the amplitude or the duration, was varied in order to analyze its influence on the dislocations' jumps.

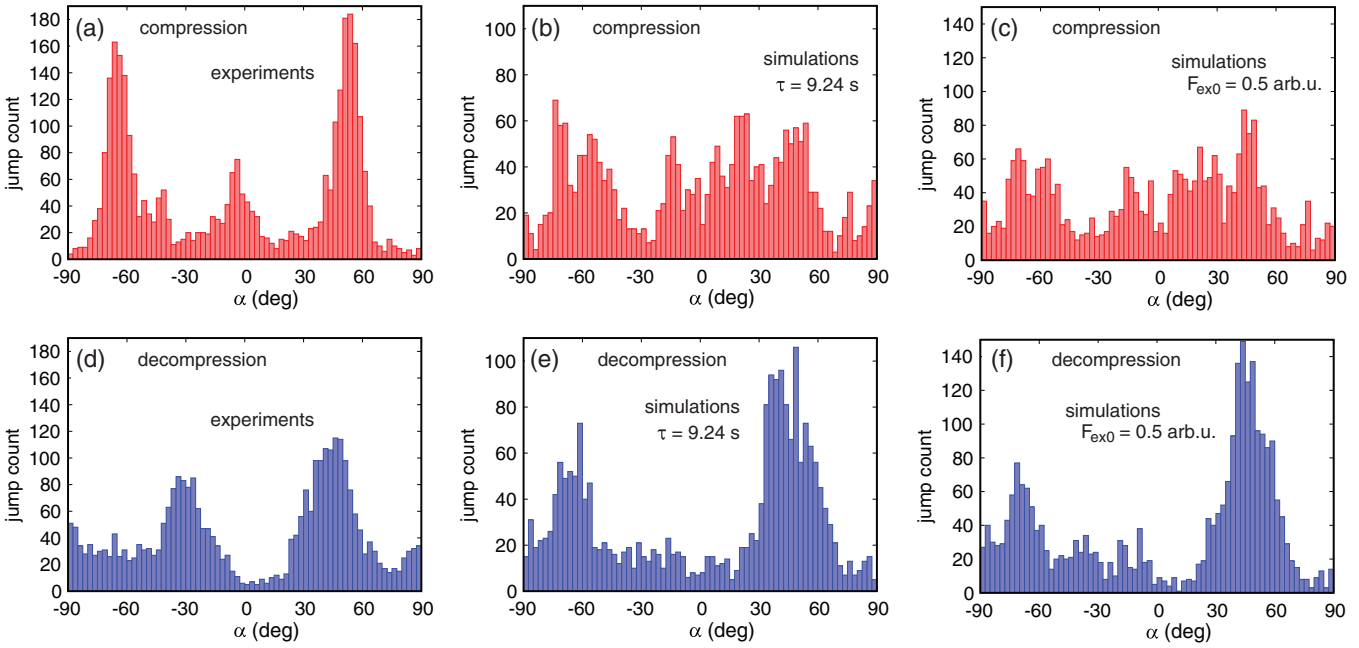

FIG. 12. (Color online) Histograms of the angle between the direction of the dislocation jump and the applied compressive force α. (a, d) Experimental runs with the rise and fall time of $\tau = 1$, 2, 3.3, 5, 10, and 20 s. (b, e) Simulation runs with the rise and fall time of $\tau = 9.24$ s and the excitation amplitudes of $F_{\rm ex0} = 0.05$, 0.1, 0.25, 0.5, 0.75, and 1.0 arb. unit. (c, f) Simulation runs with the excitation amplitude $F_{\rm ex0} = 0.5$ arb. unit and the rise and fall time of $\tau = 2.31$, 4.62, 9.24, 11.55, and 13.86 s. Panels (a–c) show compression parts, and panels (d–f) show decompression parts of the runs. The histograms were obtained using bins of 2.5°.

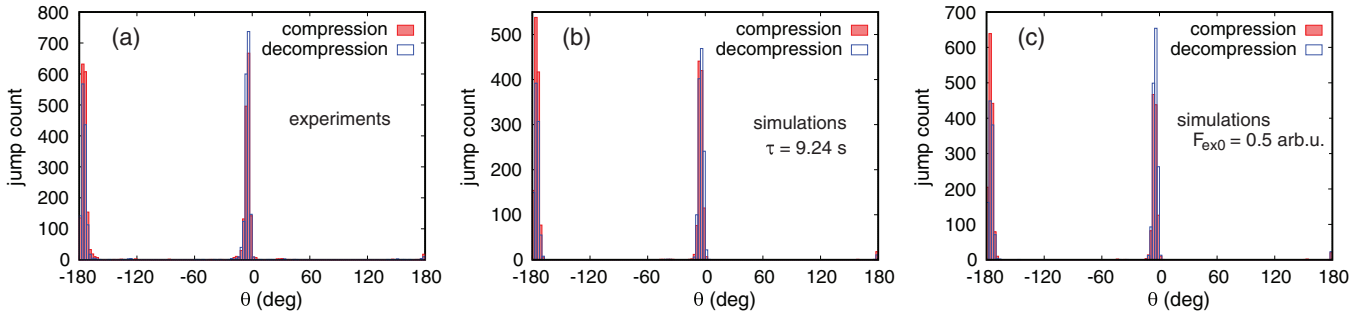

FIG. 13. (Color online) Histograms of the angle between the direction of the dislocation jump and the Burgers vector of the dislocation θ. (a) Experimental runs with the rise and fall time of $\tau = 1$, 2, 3.3, 5, 10, and 20 s. (b) Simulation runs with the rise and fall time of $\tau = 9.24$ s and the excitation amplitudes of $F_{ex0} = 0.05$, 0.1, 0.25, 0.5, 0.75, and 1.0 arb. unit. (c) Simulation runs with the excitation amplitude $F_{ex0} =$ 0.5 arb. unit and the rise and fall time of $\tau = 2.31$, 4.62, 9.24, 11.55, and 13.86 s. The histograms were obtained using bins of 2.5°. The data show that the jumps occur either in the direction of the Burgers vector or in the opposite direction.

The compression part of the experimental runs showed more defined peaks than the decompression part, but the probability associated with each binned angle in each individual experimental run was quite low, 12% at most. We also noticed a broadening of the distribution during the decompression stage, reaching a lower maximum probability of 9.4%.

For the simulations, the decompression part showed more defined peaks than the compression part (see Fig. 3). The distributions shown in Figs. 12(b) and 12(c), obtained by varying, respectively, the amplitude or the duration of the excitation force, were similar with slightly different count numbers for each angle.

The different distributions of angles between the histograms associated with both parts of the experiments and simulations confirm that there was no symmetry between the two phases of the lattices' deformations. This difference between the two parts of the runs has several causes: (i) the lattice had been deformed by the load, resulting in a different orientation of the crystalline structure and a possible rotation of subdomains of the crystal, and (ii) the hopping or jumping dislocations were different and therefore so were their Burgers vectors because of the occurrence of some generation and annihilation processes between defects.

4. Direction of the jump with respect to the dislocation's Burgers vector

Figure 13 shows the distribution of the angles θ between the PHDs' Burgers vectors and the directions of their jumps during the compression and decompression parts for (a) all experimental runs and all simulations with (b) different amplitudes (six runs) of the excitation force and (c) different durations (five runs) of the excitation force. These histograms show narrow and localized distributions of θ around 0 and $\pm 180°$ with a probability for each run comprised between 18 and 37% in the experiments and 20 and 45% in the simulations. This figure clearly shows that the jumps occurred mostly in the direction parallel or antiparallel to the dislocation's Burgers vector. During the jumps, the orientation of the Burgers vector varied by 10° on average.

Nosenko *et al.* used this property of dislocations' dynamics to perform their experiments: the authors aligned the laser beams with a principal lattice axis of complex plasma crystals. This way, the dislocations' motion in a controlled shear stress field is quasi-one-dimensional [35], and in 2D colloidal crystals stressed through an imposed chemical gradient Pertsinidis and Ling could determine the direction of the applied stress from the directions of the dislocations' jumps [38].

Finally, the different counts between the compression and decompression parts in Fig. 13 underline the fact that the deformations were plastic at the microscopic scale.

IV. CONCLUSION

We have reported experimental and numerical analysis of free dislocations' dynamics in two-dimensional complex plasma crystals submitted to a cycle of compression, constant compressed, decompression, and constant decompressed loads. Varying different experimental and numerical parameters has enabled us to analyze quasistatic as well as large deformations in these lattices. We have focused on dislocations' concentrations and their dynamics during elastic deformations and jumps, as well as on the influence of the excitation force's characteristics on the dislocations' jumps.

The jumps or glides of dislocations were mostly in the direction of the dislocation's Burgers vector. The concentration of dislocations was sensitive to the excitation force, as a high amplitude or short-duration perturbation would generate many defects preventing the generation or motion of dislocations and favoring the formation of clusters or chains of defects instead. The deformation was reversible at the macroscopic scale, as the lattice regained its original dimensions once the load was canceled. However, the microscopic deformation was plastic, as the dislocations's trajectories during both parts of the experimental and simulated runs did not overlap, showing that the deformation was not reversible at this scale.

This point has analogies with effects observed in material science, where dislocation dynamics can explain effects like strain aging and fragilization and could be exploited to modify material properties.

ACKNOWLEDGMENTS

We thank the Engineering and Physical Sciences Research Council of the United Kingdom for financial support (Grants No. EP/E04526X/1 and No. EP/G007918), and we appreciate funding from the European Research Council (ERC) under the European Unions Seventh Framework Programme (FP7/20072013)/ERC Grant Agreement 267499.

[1] *Introduction to Dislocations*, edited by D. Hull and D. J. Bacon (Butterworth-Heinemann, Oxford, 2001).
[2] G. Cicero, L. Pizzagalli, and A. Catellani, Phys. Rev. Lett. **89**, 156101 (2002).
[3] M. Payne, M. P. Teter, D. C. Allan, T. A. Arias, and J. D. Joannopoulos, Rev. Mod. Phys. **64**, 1045 (1992).
[4] S. Bhowmick and U. V. Waghmare, Phys. Rev. B **81**, 155416 (2010).
[5] M. Verdier, M. Fivel, and I. Groma, Modelling Simul. Mater. Sci. Eng. **6**, 755 (1998).
[6] J. Deng and A. El-Azab, Modelling Simul. Mater. Sci. Eng. **17**, 075010 (2009).
[7] H. Zhang, P. Kalvapalle, and J. Douglas, J. Phys. Chem. B **115**, 14068 (2011).
[8] V. Bulatov and W. Cai, *Computer Simulations of Dislocations* (Oxford University Press, Oxford, 2006).
[9] S. Groh and H. M. Zbib, J. Eng. Mater. Technol. **131**, 041203 (2009).
[10] E. R. Weeks, J. C. Crocker, A. C. Lewitt, A. Schofield, and D. A. Weitz, Science **287**, 627 (2000).
[11] C. Eisenmann, C. Kim, J. Mattsson, and D. A. Weitz, Phys. Rev. Lett. **104**, 035502 (2010).
[12] Y. Tang, A. J. Armstrong, R. C. Mockler, and W. J. O'Sullivan, Phys. Rev. Lett. **62**, 2401 (1989).
[13] A. Libál, C. Reichhardt, and C. J. Olson Reichhardt, Phys. Rev. E **75**, 011403 (2007).
[14] A. Pertsinidis and X. S. Ling, Nature (London) **413**, 147 (2001).
[15] K. Q. Zhang and X. Liu, Nature (London) **429**, 739 (2004).
[16] X. H. Zheng and R. Grieve, Phys. Rev. B **73**, 064205 (2006).
[17] A. M. Kraynik, D. A. Reinelt, and F. van Swol, Phys. Rev. E **67**, 031403 (2003).
[18] A. Kabla and G. Debrégeas, Phys. Rev. Lett. **90**, 258303 (2003).
[19] M. Lundberg, K. Krishan, N. Xu, C. S. O'Hern, and M. Dennin, Phys. Rev. E **77**, 041505 (2008).
[20] M. Dennin, Phys. Rev. E **70**, 041406 (2004).
[21] C. Durniak, D. Samsonov, S. Zhdanov, and G. Morfill, Europhys. Lett. **88**, 45001 (2009).
[22] D. Samsonov, A. V. Ivlev, R. A. Quinn, G. Morfill, and S. Zhdanov, Phys. Rev. Lett. **88**, 095004 (2002).
[23] C. Durniak, D. Samsonov, N. P. Oxtoby, J. F. Ralph, and S. Zhdanov, IEEE Trans. Plasma Sci. **38**, 2412 (2010).
[24] A. Melzer, A. Homann, and A. Piel, Phys. Rev. E **53**, 2757 (1996).
[25] C. A. Knapek, D. Samsonov, S. Zhdanov, U. Konopka, and G. E. Morfill, Phys. Rev. Lett. **98**, 015004 (2007).
[26] T. E. Sheridan, Phys. Plasmas **15**, 103702 (2008).
[27] V. Nosenko and S. K. Zhdanov, Contrib. Plasma Phys. **49**, 191 (2009).
[28] D. Samsonov, J. Goree, Z. W. Ma, A. Bhattacharjee, H. M. Thomas, and G. E. Morfill, Phys. Rev. Lett. **83**, 3649 (1999).
[29] L. Couëdel, D. Samsonov, C. Durniak, S. Zhdanov, H. M. Thomas, G. E. Morfill, and C. Arnas, Phys. Rev. Lett. **109**, 175001 (2012).
[30] B. Klumov, Physics Uspekhi **53**, 1503 (2010).
[31] C.-L. Chan, C.-W. Io, and L. I, Contrib. Plasma Phys. **49**, 215 (2009).
[32] C. Durniak and D. Samsonov, Europhys. Lett. **90**, 45002 (2010).
[33] D. Samsonov, C. Durniak, C. Knapek, and G. E. Morfill, IEEE Trans. Plasma Sci. **39**, 2738 (2011).
[34] C. A. Knapek, C. Durniak, D. Samsonov, and G. E. Morfill, AIP Conf. Proc. **1397**, 361 (2011).
[35] V. Nosenko, G. E. Morfill, and P. Rosakis, Phys. Rev. Lett. **106**, 155002 (2011).
[36] S. K. Zhdanov, M. H. Thoma, C. A. Knapek, and G. E. Morfill, New J. Phys. **14**, 023030 (2012).
[37] A. Pertsinidis and X. S. Ling, Phys. Rev. Lett. **87**, 098303 (2001).
[38] A. Pertsinidis and X. S. Ling, New J. Phys. **7**, 33 (2005).
[39] C. Durniak and D. Samsonov, Phys. Rev. Lett. **106**, 175001 (2011).
[40] P. Harvey, C. Durniak, D. Samsonov, and G. Morfill, Phys. Rev. E **81**, 057401 (2010).
[41] D. Samsonov, S. K. Zhdanov, R. A. Quinn, S. I. Popel, and G. E. Morfill, Phys. Rev. Lett. **92**, 255004 (2004).
[42] W. Press, S. Teukolsky, W. Vetterling, and B. Flannery, *Numerical Recipes in C: The Art of Scientific Computing*, 2nd ed. (Cambridge University Press, Cambridge, 1992).
[43] M. Petrou and P. Bosdogianni, *Image Processing the Fundamentals* (Wiley, New York, 1999).
[44] R. Haralick, S. Sternberg, and X. Zhuang, IEEE Transactions on Pattern Analysis and Machine Intelligence **9**, 532 (1987).
[45] Y. Feng, J. Goree, and B. Liu, Rev. Sci. Instrum. **78**, 053704 (2007).
[46] Y. Ivanov and A. Melzer, Rev. Sci. Instrum. **78**, 033506 (2007).
[47] N. P. Oxtoby, J. F. Ralph, C. Durniak, and D. Samsonov, Phys. Plasmas **19**, 013708 (2012).
[48] C. Kittel, *Introduction to Solid State Physics*, 2nd ed. (Wiley, New York, 1961).
[49] A more formal definition of the Burgers vector invokes the concept of corresponding paths in the real crystal and in a defect-free reference crystal. The sign of the Burgers vector is not defined until a positive direction has been arbitrarily assigned to the line, and even then either of two opposite conventions may be used [69]. In what follows we accepted the definition proposed by Eisenmann *et al.* [70]. Note that in [37,38] an opposite convention has been introduced.
[50] A tracking procedure for compact dislocation clusters and other point defects associations has been proposed in [36].
[51] A. Stukowski and K. Albe, Modelling Simul. Mater. Sci. Eng. **18**, 025016 (2010).

[52] V. Nosenko, J. Goree, and A. Piel, Phys. Plasmas **13**, 032106 (2006).
[53] M. A. Shehadeh, H. M. Zbib, and T. Diaz de la Rubia, International Journal of Plasticity **21**, 2369 (2005).
[54] V. Steinberg, R. Sütterlin, A. V. Ivlev, and G. Morfill, Phys. Rev. Lett. **86**, 4540 (2001).
[55] R. A. Quinn and J. Goree, Phys. Rev. E **64**, 051404 (2001).
[56] M. Kong, B. Partoens, and F. M. Peeters, Phys. Rev. E **67**, 021608 (2003).
[57] V. Nosenko, S. Zhdanov, and G. Morfill, Phys. Rev. Lett. **99**, 025002 (2007).
[58] V. Nosenko, S. K. Zhdanov, and G. Morfill, Philos. Mag. **88**, 3747 (2008).
[59] S. Chen, E. Ertekin, and D. C. Chrzan, Phys. Rev. B **81**, 155417 (2010).
[60] M. L. Wallace and B. Joos, J. Phys.: Condens. Matter **20**, 244130 (2008).
[61] M. Robles, V.Mustonen, and K. Kaski, Int. J. Modern Physics C **14**, 407 (2003).
[62] V. V. Bulatov, L. L. Hsiung, M. Tang, A. Arsenlis, M. C. Bartelt, W. Cai, J. N. Florando, M. Hiratani, M. Rhee, G. Hommes, T. G. Pierce, and T. Diaz de la Rubia, Nature (London) **440**, 1174 (2006).
[63] R. J. Amodeo and N. M. Ghoniem, Phys. Rev. B **41**, 6958 (1990).
[64] R. Madec, B. Devincre, L. Kubin, T. Hoc, and D. Rodney, Science **301**, 1879 (2003).
[65] E. M. Bringa, K. Rosolankova, R. E. Rudd, B. A. Remongton, J. S. Wark, M. Duchaineau, D. H. Kalantar, J. Hawreliak, and J. Belak, Nature Materials **5**, 805 (2006).
[66] M. Robles, L. Perondi, and K. Kaski, Int. J. Modern Physics C **13**, 97 (2002).
[67] B. Devincre, T. Hoc, and L. Kubin, Science **320**, 1745 (2008).
[68] T. Richeton, J. Weiss, and F. Louchet, Acta Mater. **53**, 4463 (2005).
[69] J. W. Christiam and V. Vitek, Rep. Prog. Phys. **33**, 307 (1970).
[70] C. Eisenmann, U. Gasser, P. Keim, G. Maret, and H. H. von Grünberg, Phys. Rev. Lett. **95**, 185502 (2005).